

Learned Turbulence Modelling with Differentiable Fluid Solvers

Björn List, Li-Wei Chen, Nils Thuerey

Departement of Informatics, Technical University of Munich

February 16, 2022

Abstract

In this paper, we train turbulence models based on convolutional neural networks. These learned turbulence models improve under-resolved low resolution solutions to the incompressible Navier-Stokes equations at simulation time. Our method involves the development of a differentiable numerical solver that supports the propagation of optimisation gradients through multiple solver steps. We showcase the significance of this property by demonstrating the superior stability and accuracy of those models that featured a higher number of unrolled steps during training. This approach is applied to three two-dimensional turbulence flow scenarios, a homogeneous decaying turbulence case, a temporally evolving mixing layer and a spatially evolving mixing layer. Our method achieves significant improvements of long-term *a-posteriori* statistics when compared to no-model simulations, without requiring these statistics to be directly included in the learning targets. At inference time, our proposed method also gains substantial performance improvements over similarly accurate, purely numerical methods.

1 Introduction

Obtaining accurate numerical solutions to turbulent fluid flows remains a challenging task, and is subject to active research efforts not only in the domain of fluid dynamics [Argyropoulos and Markatos, 2015], but also other fields including climate research [Aizinger et al., 2015] and the medical sciences [Bozzi et al., 2021]. Direct Numerical Simulation (DNS), which attempts to fully resolve the vast scale of turbulent motion, is prohibitively expensive in many flow scenarios, and is thus often adverted by using turbulence models. For instance, Reynolds-Averaged-Navier-Stokes (RANS) modelling has successfully been deployed to complex flow problems such as aircraft shape design and optimisation of turbo-machinery [Argyropoulos and Markatos, 2015]. However, the temporally averaged solutions obtained from RANS modelled simulations lack concrete information about instantaneous vortex movements in the flow. Thus, Large Eddy Simulation (LES) constitutes another common choice for turbulence modelling, providing a time-sensitive perspective to the turbulent flows [Pope, 2004]. The computational expense of LES is nevertheless still substantial, and their applicability therefore remains restricted [Choi and Moin, 2012; Slotnick et al., 2014; Yang, 2015].

The persistent challenges of traditional approaches motivate the use of machine learning, in particular deep learning, for turbulence modelling [Duraisamy et al., 2019]. The reduced complexity of steady-state RANS made these setups a promising target for early efforts of machine learning based turbulence. As a result, substantial progress has been made towards data-driven prediction of the RANS flow fields, vastly outperforming pure numerical solvers in the process [Bhatnagar et al., 2019; Thuerey et al., 2020].

Similar efforts were targeted towards the data-driven development of LES models. One of the earliest works showcased the capability of neural networks to reproduce the turbulent viscosity coefficient [Sarghini et al., 2003]. Furthermore, Maulik et al. [2019] proposed a supervised

machine learning method to infer the subgrid-scale (SGS) stress tensor from the flow field, and achieved promising results on the two-dimensional decaying turbulence test cases. Herein, the *a-priori* evaluations served as a learning target and could be accurately reproduced, however *a-posteriori* evaluations were not always in direct agreement. Beck et al. [2019] trained a data-driven closure-model based on a Convolutional Neural Network (CNN) and demonstrated good accuracy at predicting the closure on a three-dimensional homogeneous turbulence case, albeit stating that using their trained model in LES is not yet possible. Related prediction capabilities with trade-offs in terms of model stability of a similar supervised approach were reported in [Cheng et al., 2019]. Xie et al. [2019] utilised a similar approach on compressible flows, later expanding their method to multi-scale filtering [Xie et al., 2020]. Park and Choi [2021] studied possible formulations for the input to the neural network and evaluated their results on a turbulent channel flow.

Beyond the supervised learning approaches covered so far, Novati et al. [2021] proposed a multi-agent reinforcement learning approach, where the LES viscosity coefficient was inferred by local agents distributed in the numerical domain. Their turbulence model achieved good results when applied to a forward simulation. From these previous studies on machine learning based turbulence models, two fundamental observations solidify. Firstly, the parametric range of sufficiently large networks can be trained to identify and differentiate turbulent structures and draw modelling conclusions from these structures. Secondly, the feedback from supervised training formulations cannot express the long term effects of these modelling decisions, and thus cannot provide information about the temporal stability of a model. While the reinforcement learning approach provides long temporal evolutions, its explorative nature makes this method computationally expensive. To exploit the benefits of data-driven training like supervised models, and simultaneously provide training feedback over long time horizons, a deeper integration of neural network models in numerical solvers is necessary.

In contrast to the supervised learning approaches, further research proposed to realise this deep integration by training neural networks through differentiable solvers and adjoint optimisation for partial differential equations. These works initially focused on learning-based control tasks [de Avila Belbute-Peres et al., 2018; Holl et al., 2020]. By combining differentiable solvers with neural network models, optimisation gradients can propagate through solver steps and network evaluations [Thuerey et al., 2021]. This allows for targeting loss formulations that require a temporal evolution of the underlying partial differential equation. In the following, we will refer to approaches characterised by this integration of neural networks into numerical solvers as *hybrid methods*. These techniques were shown to overcome the stability issues of supervised methods, and thus provided a basis for learned turbulence models in unsteady simulations. By integrating CNNs into the numerical solver, Um et al. [2020] found models to improve with increased time horizons seen during training, which resulted in a stable learned correction function that was capable of efficiently improving numerical solutions to various partial differential equations. Similarly, Kochkov et al. [2021] found differentiable solver architectures to be beneficial for training turbulence models. While this work estimates substantial performance gains over traditional techniques for first-order time integration schemes, we will evaluate a different solver that is second-order in time, putting more emphasis on an evaluation with appropriate metrics from fluid mechanics.

In another related approach, Sirignano et al. [2020] proposed a learned correction motivated by turbulence predictions in LES of isotropic turbulence, and later expanded on this by studying similar models in planar jets [MacArt et al., 2021]. Here, *a-posteriori* statistics served as a training target, however, without investigating the temporal effects of hybrid solvers and their training methodologies in more detail.

In this paper, we seek to develop further understanding of turbulence modelling with hybrid learned approaches. In an effort to bridge the gap between previously mentioned papers we want to address a series of open questions. Firstly, no single unified learning approach has been applied

to a range of turbulent flow scenarios. Secondly, there is little information on the choice of loss functions for turbulence models in specific flow scenarios. Thirdly, it has not been studied in detail how the number of unrolled steps seen during training affects the neural network models’ *a-posteriori* behaviour. In order to provide insights to these questions, we utilise a CNN to train a corrective forcing term through a differentiable solver, which allows an end-to-end training that is flexible towards the number of unrolled steps, loss formulations and training targets. We then show that the same network architecture can achieve good accuracy with respect to *a-posteriori* metrics of three different flow scenarios. In our method, we relax the timestep requirements usually found in unsteady turbulence modelling, such as LES, by downscaling our simulations such that a constant Courant-Friedrichs-Lowy (CFL) ratio is maintained. By implication, a learned model is trained to (i) take the classical sub-grid scale closure into account, (ii) approximate temporal effects, and (iii) correct for discretisation errors. Our models are trained and evaluated on three different, two-dimensional flow cases: the isotropic decaying turbulence, a temporally developing mixing layer as well as the spatially developing mixing layer. We show that in all cases, training a turbulence model through an increasing number of unrolled solver steps enhances the model accuracy and thus demonstrate the benefits of a differentiable solver. Furthermore, our results indicate that accurate models with respect to *a-posteriori* turbulence statistics are achieved without directly using them as training targets. Nonetheless, a loss formulation inspired by *a-posteriori* evaluations is shown to yield further improvements. Finally, we provide a performance analysis of our models that measures speed-ups of up to 14 with respect to comparably accurate solutions from traditional solvers.

The remainder of this paper is organised as follows. In section 2, we introduce an overview of our methodology and the solver-network interaction. A description and evaluation of experiments with the isotropic decaying turbulence case is found in section 3, which is followed by similar studies regarding the temporally developing mixing layer and the spatially developing mixing layer in sections 4 and 5 respectively. A comparison of computational costs at inference time can be found in section 6, while section 7 contains concluding thoughts.

2 Learning Turbulence Models

In this paper, we study neural networks for turbulence modelling in incompressible fluids. These flows are governed by the Navier-Stokes equations

$$\begin{aligned} \frac{\partial \mathbf{u}}{\partial t} + \mathbf{u} \cdot \nabla \mathbf{u} &= -\nabla p + \frac{1}{Re} \nabla^2 \mathbf{u} + \mathbf{f}, \\ \nabla \cdot \mathbf{u} &= 0, \end{aligned} \tag{1}$$

where $\mathbf{u} = [u \ v]^T$, p and Re are the velocity field, pressure field and Reynolds number respectively. The term $\mathbf{f} = [f_x \ f_y]^T$ represents an external force on the fluid. In the context of turbulent flows, an accurate solution to these equations entails either resolving and numerically simulating all turbulent scales, or modelling the turbulence physics through an approximative model.

Our aim is to develop a method that enhances fluid simulations by the means of a machine learning model. In particular, we aim to improve the handling of fine temporal and spatial turbulence scales that are potentially under-resolved, such that the influence of these scale on the larger resolved motions needs to be modelled. The function that approximates these effects is solely based on the low resolution data and is herein parameterised by a CNN. The network is then trained to correct a low-resolution numerical solution during the simulation, such that the results coincides with a downsampled high-resolution dataset. Within this hybrid approach, the turbulence model directly interacts with the numerical solver at training and at inference time. To achieve this objective, we utilise differentiable solvers, i.e., solvers which provide derivatives with

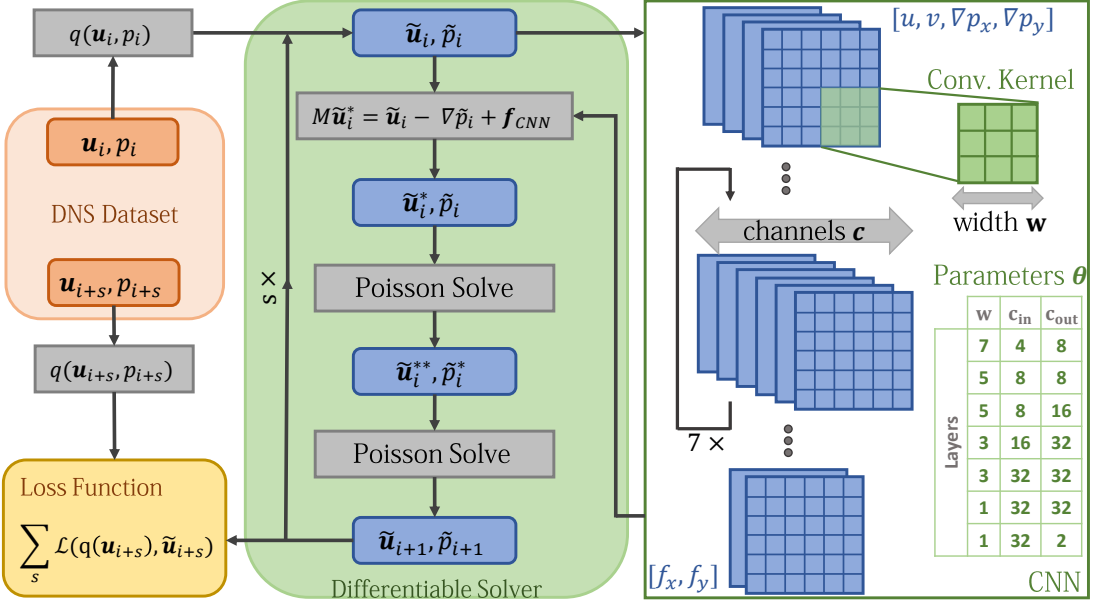


Figure 1: Solver procedure of the PISO-scheme and its interaction with the convolutional neural network.

respect to their output state. Such solvers can be seen as part of the differentiable programming methodology in deep learning, which is equivalent to employing the adjoint method from classical optimisation [Giles et al., 2003] in the context of neural networks. The differentiability of the solver enables the propagation of optimisation gradients through multiple solver steps and neural network evaluations.

2.1 Differentiable PISO solver

Our differentiable solver is based on the semi-implicit PISO-scheme introduced by Issa [1986], which has been used for a wide range of flow scenarios [Barton, 1998; Kim and Benson, 1992]. Each second-order time integration step is split into an implicit predictor step solving the discretised momentum equation, followed by two corrector steps that ensure the incompressibility of the numerical solution to the velocity field. The Navier-Stokes equations are discretised using the Finite-Volume method, while all cell fluxes are computed to second-order accuracy.

The solver is implemented on the basis of *TensorFlow* [Abadi et al., 2016], which facilitates parallel execution of linear algebra operations on the Graphics Processing Unit (GPU), as well as differentiability of said operations. Additional functions exceeding the scope of TensorFlow (TF) are written as custom operations and implemented using CUDA. This approach allows us to seamlessly integrate initially unsupported features such as sparse matrix operations in the TF-graph. More details about the solver structure and implementation can be found in appendix A. Figure 1 gives a brief overview of the solver procedure. In the following, we will denote a PISO solver step \mathcal{S} as

$$(\mathbf{u}_{i+1}, p_{i+1}) = \mathcal{S}(\mathbf{u}_i, p_i, \mathbf{f}_i) \quad (2)$$

where \mathbf{u}_i, p_i and \mathbf{f}_i represent discretised velocity, pressure and forcing fields at a time t_i .

2.2 Neural Network Architecture

Turbulence physics strongly depends on the local neighbourhood. Thus, the network has to infer the influence of unresolved scales for each discrete location based on the surrounding flow fields. This physical relation can be represented by discrete convolutions, where each output

value is computed based solely on the surrounding computational cells as well as a convolutional weighting kernel. This formulation introduces a restricted receptive field for the convolution and ensures the local dependence of its output [Luo et al., 2016]. Chaining multiple of these operations results in a deep CNN, which was successfully used in many applications ranging from computer vision and image recognition [Albawi et al., 2017] to fluid mechanics and turbulence research [Beck et al., 2019; Guastoni et al., 2021; Lapeyre et al., 2019]. We use a fully convolutional network with 7 convolutional layers and leaky ReLU activations, containing $\sim 82 \times 10^3$ trainable parameters. As illustrated in figure 1, our CNN takes the discretised velocity and pressure gradient fields as input. This formulation contains full information of the field variable states, and enables the modelling of both temporal and spatial effects of turbulence, as well as correction of numerical inaccuracies. However, any principles of the modelled physics, like Galilean invariance in the case of SGS-closure, must be learnt by the network itself. The choice of network inputs is by no means trivial, but shall not be further studied in this paper. Refer to [Choi and Moin, 2012; MacArt et al., 2021; Xie et al., 2019, 2020] for in-depth analyses. The output of our networks is conditioned on its weights θ , and can be interpreted as a corrective force $\mathbf{f}_{\text{CNN}}(\mathbf{u}_i, p_i | \theta) : (\mathbb{R}^2, \mathbb{R}) \rightarrow \mathbb{R}^2$ to the under-resolved simulation of the Navier-Stokes equations (1). This force directly enters the computational chain at PISO’s implicit predictor step. As a consequence, the continuity equation is still satisfied at the end of a solver step, even if the simulation is manipulated by the network forcing. For a detailed description of the network structure, including CNN kernel sizes, initialisations and padding, refer to appendix B.

2.3 Unrolling Timesteps for Training

Our method combines the numerical solver introduced in section 2.1 with the modelling capabilities of CNNs as outlined in 2.2. As also illustrated in figure 1, the resulting data-driven training algorithm works based on a dataset $(\mathbf{u}(t_i), p(t_i))$ consisting of high-resolution velocity fields $\mathbf{u}(t_i) \in \mathbb{R}^n$ and corresponding pressure fields $p(t_i) \in \mathbb{R}$ for the discrete time t_i . In order to use this DNS data for training underresolved simulations on different grid resolutions, we define a down-sampling procedure $q(\mathbf{u}, p) : (\mathbb{R}^2, \mathbb{R}) \rightarrow (\mathbb{R}^2, \mathbb{R})$, that takes samples from the dataset and outputs the data $(\tilde{\mathbf{u}}_i, \tilde{p}_i)$ at a lower target-resolution via bilinear interpolation. This step performs an implicit filtering on the DNS data, which is used to generate input and target frames of an optimisation step. For the sake of simplicity, we will denote a downsampled member of the dataset consisting of velocities and pressure as $\tilde{q}_i = q(\mathbf{u}(t_i), p(t_i))$. Similarly, we will write $\tilde{\mathbf{f}}_i = \mathbf{f}_{\text{CNN}}(\tilde{\mathbf{u}}_i, \tilde{p}_i | \theta)$. Note that the network operates solely on low-resolution data and introduces a corrective forcing to the low-resolution simulation, with the goal of reproducing the behaviour of an implicitly filtered DNS. We formulate the training objective as

$$\min_{\theta} (\mathcal{L}(\tilde{q}_{i+\tau}, \mathcal{S}_{\tau}(\tilde{q}_i, \tilde{\mathbf{f}}_i))), \quad (3)$$

for a loss function \mathcal{L} that satisfies $\mathcal{L}(x, y) \rightarrow 0$ for $x \approx y$. By this formulation, the network should output a forcing such that the flow fields resulting from a low-resolution solver step closely resemble the next downsampled frame, when given a downsampled DNS snapshot. The temporal increment τ between these subsequent frames is set to match the timesteps in the low-resolution solver \mathcal{S} , which in turn are tuned to maintain Courant numbers identical to the DNS.

Um et al. [2020] showed that similar training tasks benefit from unrolling multiple temporal integration steps in the optimisation loop. Through this procedure, the optimisation can account for longer term effects of the network output on the temporal evolution of the solution, increasing accuracy and stability in the process. We utilise the same technique and find it to be critical for the long-term stability of turbulence models. Our notation from equations (2) and (3) is extended to generalise our approach to work with multiple subsequent snapshots. When training a model

through n unrolled steps, the optimisation objective becomes

$$\min_{\theta} \left(\sum_s \mathcal{L}(\tilde{q}_{i+s\tau}, \mathcal{S}_\tau^s(\tilde{q}_i, \tilde{\mathbf{f}}_i)) \right), \quad (4)$$

where \mathcal{S}^s denotes the successive execution of s solver steps including network updates, starting with the initial fields q_i . By this formulation the optimisation works towards matching not only the final, but also all intermediate frames.

2.4 Loss Functions

As introduced in equation (3), the training of deep CNNs is an optimisation of its parameters. The loss function \mathcal{L} serves as the optimisation objective and thus has to assess the quality of the network output. Since our approach targets the reproduction of DNS-like behaviour on a coarse grid, the chosen loss function should consequently aim to minimise the distance between the state of a modelled coarse simulation and the DNS. In this context, a natural choice is the \mathcal{L}_2 -loss

$$\mathcal{L}_2 = \sqrt{(\tilde{\mathbf{u}} - q(\mathbf{u})) \cdot (\tilde{\mathbf{u}} - q(\mathbf{u}))}, \quad (5)$$

since this formulation drives the optimisation towards resembling a desired outcome. Therefore, the \mathcal{L}_2 -loss trains the network to directly reproduce the downsampled high-resolution fields, and the perfect reproduction from an ideal model gives $\mathcal{L}_2 = 0$. Since the differentiable solver allows us to unroll multiple simulation frames, we apply this loss formulation across a medium-term time horizon and thus also optimise towards multi-step effects. By providing a large quantity of sections from our DNS dataset to the optimisation, we implicitly train a turbulence model that represents the unresolved scales on the basis of local turbulent features. While the \mathcal{L}_2 -loss described in 5 has its global minimum when the DNS behaviour is perfectly reproduced, in practice, we find that it can neglect the time evolution of certain fine scale, low amplitude features of the solutions. This property of the \mathcal{L}_2 -loss is not unique to turbulence modelling and has previously been observed in machine learning in other scientific fields such as computer vision Yu et al. [2018]. To alleviate these shortcomings, we include additional loss-formulations, which alter the loss-landscape to avoid these local minima.

We define a spectral energy loss \mathcal{L}_E , designed to improve the accuracy of the learned model on fine spacial scales. It is formulated as the log-spectral distance of the spectral kinetic energies

$$\mathcal{L}_E = \sqrt{\int_k \log \left(\frac{\tilde{E}(k)}{E^q(k)} \right)^2 dk}, \quad (6)$$

where $\tilde{E}(k)$ denotes the spectral kinetic energy of the low-resolution velocity field at wavenumber k , and E^q represents the same quantity for the downsampled DNS data. In practice, this loss formulation seeks to equalise the kinetic energy in the velocity field for each discrete wavenumber. The log-rescaling of the two respective spectra regularises the relative influence of different spatial scales. This energy loss elevates the relative importance of fine scale features.

Our final aim is to train a model that can be applied to a standalone forward simulation. The result of a neural network modelled low-resolution simulation step should therefore transfer all essential turbulence information, such that the same model can once again be applied in the subsequent step. The premises of modelling the unresolved behaviour are found in the conservation equation for the implicitly filtered low-resolution kinetic energy in tensor notation

$$\frac{\partial \tilde{E}_f}{\partial t} + \tilde{u}_i \frac{\partial \tilde{E}_f}{\partial x_i} + \frac{\partial}{\partial x_j} \tilde{u}_i [\delta_{ij} \tilde{p} + \tau_{ij}^r - \frac{2}{\text{Re}} \tilde{\mathcal{S}}_{ij}] = -\epsilon_f - \mathcal{P}^r, \quad (7)$$

where \tilde{E}_f denotes the kinetic energy of the filtered velocity field, τ_{ij}^r represents the SGS stress tensor, $\tilde{\mathcal{S}}_{ij} = \frac{1}{2}(\frac{\partial \tilde{u}_i}{\partial x_j} + \frac{\partial \tilde{u}_j}{\partial x_i})$ is the resolved rate of strain, whereas ϵ_f and \mathcal{P}^r are sink and source terms for the filtered kinetic energy. These terms are defined as $\epsilon_f = \frac{2}{Re}\tilde{\mathcal{S}}_{ij}\tilde{\mathcal{S}}_{ij}$ and $\mathcal{P}^r = -\tau_{ij}^r\tilde{\mathcal{S}}_{ij}$. The viscous sink ϵ_f represents the dissipation of kinetic energy due to molecular viscous stresses at grid-resolved scales. In our hybrid approach, this viscous dissipation at grid level ϵ_f is fully captured by the numerical solver. On the contrary, the source term \mathcal{P}^r representing the energy transfer from the resolved scales to the residual motions cannot be computed, because the SGS stresses τ_{ij}^r are unknown. One part of the modelling objective is to estimate these unresolved stresses and the interaction of filtered and SGS motions. Since the energy transfer between these scales \mathcal{P}^r depends on the filtered rate of strain \mathcal{S}_{ij}^r , special emphasis is required to accurately reproduce the filtered strain tensor. This motivates the following rate of strain loss

$$\mathcal{L}_S = \sum_{i,j} |\tilde{\mathcal{S}}_{ij} - \mathcal{S}_{ij}^q|, \quad (8)$$

where \mathcal{S}_{ij}^q denotes the rate of strain of the downsampled high-resolution velocity field. This loss term insures that the output of a hybrid solver step carries the information necessary to infer an accurate forcing in the subsequent step.

While our models primarily focus on influences of small scale motions on the large scale resolved quantities, we now draw attention to the largest scale, the mean flow. To account for the mean flow at training time, an additional loss contribution is constructed to match the multi-step statistics and written as

$$\mathcal{L}_{MS} = \| \langle \mathbf{u} \rangle_s - \langle \tilde{\mathbf{u}} \rangle_s \|_1, \quad (9)$$

where $\langle \rangle_s$ denotes an averaging over the s unrolled training steps. This notation resembles Reynolds-averaging, albeit being focused on the shorter time-horizon unrolled during training. Matching the averaged quantities is essential to achieving long-term accuracy of the modelled simulations for quasi-steady simulations, but lacks physical meaning in transient cases. Therefore, this loss contribution is solely applied to quasi-steady simulations. In this case, the rolling average $\langle \rangle_s$ approaches the steady mean flow for increasing values of s .

Our combined turbulence loss formulation as used in the network optimisations additively combines the aforementioned terms as

$$\mathcal{L}_T = \lambda_2 \mathcal{L}_2 + \lambda_E \mathcal{L}_E + \lambda_S \mathcal{L}_S + \lambda_{MS} \mathcal{L}_{MS}, \quad (10)$$

where λ denotes the respective loss factor. Their exact values are mentioned in the flow scenario specific chapters. Note that these loss terms, similar to the temporal unrolling, do not influence the architecture or computational performance of the trained neural network at inference time. They only exist at training time to guide the network to an improved state with respect to its trainable parameters. Next, we explain our experiments employing CNNs trained with this loss formulation in three different turbulence scenarios.

3 Two-Dimensional Isotropic Decaying Turbulence

Isotropic decaying turbulence in two dimensions provides an idealised flow scenario [Lilly, 1971], and is frequently used for evaluating model performance [Kochkov et al., 2021; Maulik et al., 2019; San, 2014]. It is characterised by a large number of vortices that merge at the large spatial scales whilst the small scales decay in intensity over time. We use this flow configuration to explore and evaluate the relevant parameters, most notably the number of unrolled simulation steps as well as the effects of loss formulations.

| Name | Loss | Steps | MSE at t_1 | MSE at t_2 |
|---------------------|-----------------|-------|--------------|--------------|
| LR | - | - | 2.78e-3 | 0.057 |
| LES | - | - | 2.69e-3 | 0.051 |
| NN _{sup,T} | \mathcal{L}_T | 1 | 1.52e-3 | 0.369 |
| NN _{1,T} | \mathcal{L}_T | 1 | 1.65e-3 | 0.046 |
| NN ₁₀ | \mathcal{L}_2 | 10 | 4.23e-4 | 0.018 |
| NN _{10,T} | \mathcal{L}_T | 10 | 4.25e-4 | 0.022 |
| NN _{30,T} | \mathcal{L}_T | 30 | 4.09e-4 | 0.021 |

Table 1: Training details for models trained on the isotropic turbulence case, MSE evaluated at $t_1 = 64\Delta t_{LR} \approx 5\hat{t}$ and $t_2 = 512\Delta t_{LR} \approx 40\hat{t}$

In order to generate training data, we ran a simulation on a square domain with periodic boundaries in both spatial directions. The initial velocity and pressure fields were generated using the initialisation procedure by San and Staples [2012]. The Reynolds numbers are calculated as $Re = (\hat{e}\hat{l})/\nu$, with the kinetic energy $\hat{e} = (\langle u_i u_i \rangle)^{1/2}$ and the integral length scale $\hat{l} = \hat{u}/\hat{\omega}$ and $\hat{\omega} = (\langle \omega_i \omega_i \rangle)^{1/2}$. The Reynolds number of this initialisation was $Re = 126$. The simulation was run for a duration of $T = 10^4 \Delta t_{DNS} = 100\hat{t}$, where the integral timescale is calculated as $\hat{t} = 1/\hat{\omega}$ at the initial state. During the simulation, the backscatter effect transfers turbulence energy to the larger scales, which increases the Reynolds number [Chasnov, 1997]. In our dataset, the final Reynolds number was $Re = 296$. Our aim is to estimate the effects of small scale turbulent features on a larger scale grid based on fully resolved simulation data. Consequently, the dataset should consist of a fully resolved DNS and suffice the resolution requirements. In this case the square domain $(L_x, L_y) = (2\pi, 2\pi)$ was discretised by $(N_x, N_y) = (1024, 1024)$ grid cells and the simulation evolved with a timestep satisfying $CFL = 0.3$.

We trained a series of models on downsampled data, where spatial and temporal resolution were decreased by a factor of 8. Our best performing model was trained through 30 unrolled simulation steps, which is equivalent to 2 to 3 integral timescales \hat{t} , depending on the state of the simulation. The loss factors from equation (10) were chosen as $(\lambda_2, \lambda_E, \lambda_S, \lambda_{MS}) = (10, 5 \times 10^{-2}, 1 \times 10^{-5}, 0)$.

After training, a forward simulation was run for comparison with a test dataset. These test-simulations used an initialisation different to the training data. The test simulations were advanced for $1000\Delta t = 80\hat{t}$.

We provide visual comparisons of vorticity snapshots in figure 2, where our method's improvements become apparent. The network-modelled simulations produce a highly accurate evolution of vorticity centers, and comparable performance cannot be achieved without a model for the same resolution. We also investigate the resolved turbulence kinetic energy spectra in figure 3. Whilst the no-model simulation overshoots the DNS energy at its smallest resolved scales, the learned model simulations perform better and match the desired target spectrum. Figure 4 shows temporal evolutions of the domain-wide resolved turbulence energy and the domain-wide resolved turbulence dissipation rate. The turbulence energy is evaluated according to $E(t) = \int u'_i(t)u'_i(t)d\Omega$, where u'_i is the turbulent fluctuation. We calculate the turbulence dissipation as $\epsilon(t) = \int \langle \mu \frac{\partial u'_i}{\partial x_k} \frac{\partial u'_i}{\partial x_k} \rangle d\Omega$. Simulations with our CNN models strongly agree with the downsampled DNS.

To evaluate the influence of the choice of loss function and the number of unrolled steps, several alternative models were evaluated. Additionally, we trained a model with a traditional supervised approach. In this setting, the differentiable solver is not used, and the training is performed purely on the basis of the training data set. In this case, the corrective forcing is added after a solver step is computed. The optimisation becomes

$$\min_{\theta} (\mathcal{L}(q_{i+\tau}, \mathbf{f}_{\text{CNN}}(\mathcal{S}_{\tau}(q_i))). \quad (11)$$

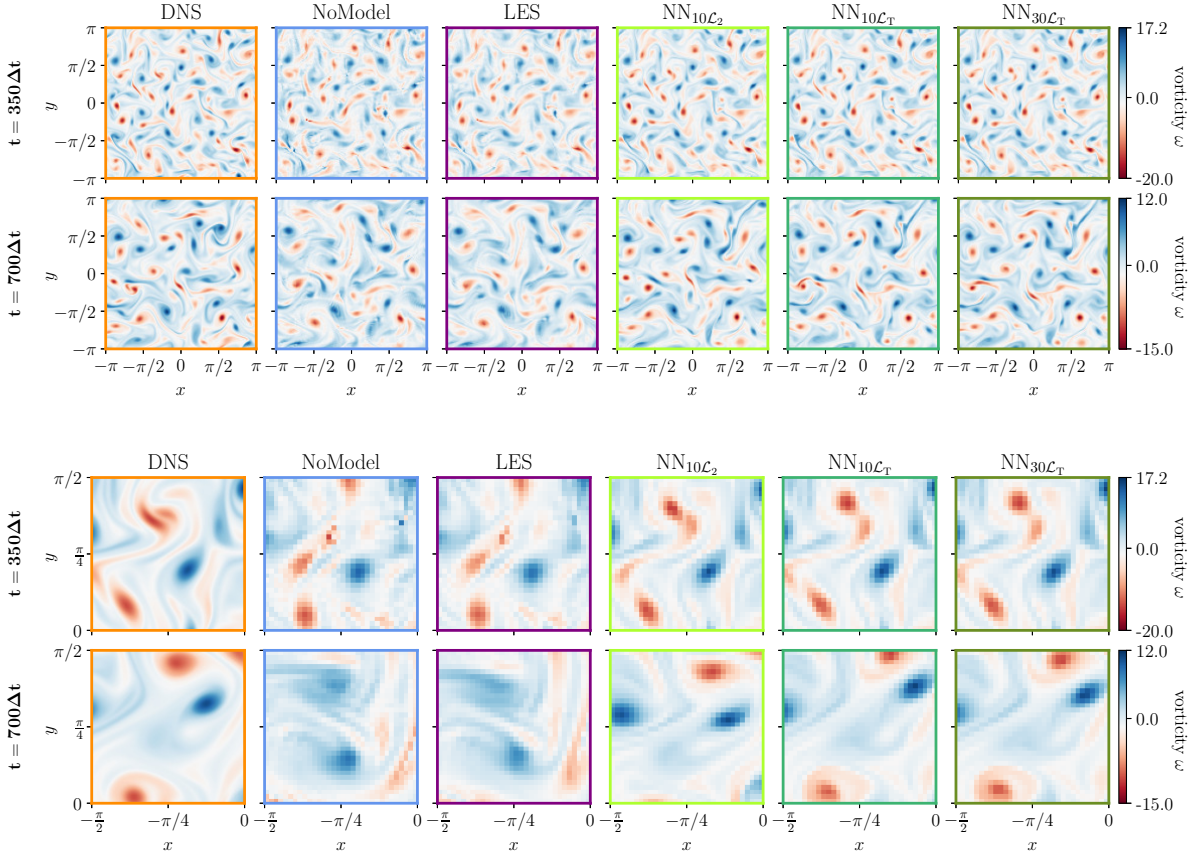


Figure 2: Vorticity visualisations of DNS, no-model, LES, and learned model simulations at $t = (350, 700)\Delta t$ on the test dataset, zoomed-in version below

Furthermore, a LES with the standard Smagorinsky model was included in the comparison. An ablation study targeting the Smagorinsky coefficient revealed that a value of $C_s = 0.008$ handles the physical behaviour of our setup best. See appendix D for details. An overview of the all models and their parameters is given in table 1. Note that the temporal advancement of the forward simulations greatly surpasses the unrolled training horizon, which leads to instabilities with the supervised and 1-step model, and ultimately to the divergence of their simulations. Consequently, we conclude that more unrolled steps are critical for the applicability of the learned models and do not include the 1-step model in further evaluations.

All remaining learned models stay in close proximity to the desired high-resolution evolutions, whereas the LES-modelled and no-model simulations significantly deviate from the target. Overall, the neural network models trained with more unrolled steps outperformed others, while the turbulence loss formulation \mathcal{L}_T also had a positive effect.

In particular, the backscatter effect is crucial for simulations of decaying turbulence. The CNN adequately dampens the finest scales as seen in the high wavenumber section of the energy spectrum (figure 3), it also successfully boosts larger scale motions. In contrast, the no-model simulation lacks dampening in the finest scales and cannot reproduce the backscatter effect on the larger ones. On the other hand, the dissipative nature of the Smagorinsky model used in the LES leads to undersized spectral energies across all scales. Especially the spectral energies of no-model and LES around wavenumber $k = 10$ show large deviations from the ground truth, while the CNN model accurately reproduces its behaviour. These large turbulent scales are the most relevant to the resolved turbulence energy and dissipation statistics, which is reflected in figure 4. Herein, the neural-network models maintain the best approximations, and high numbers of

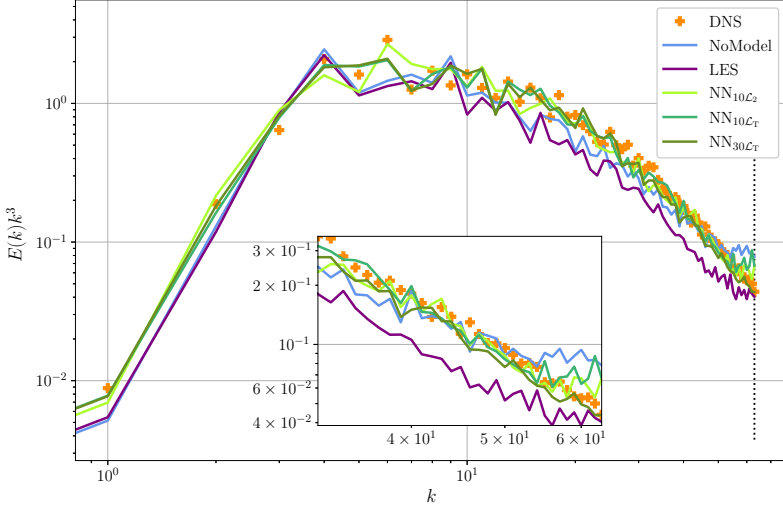


Figure 3: Resolved turbulence kinetic energy spectra of the downsampled DNS, no-model, LES, and learned model simulations; the learned 30-step model matches the energy distribution of downsampled DNS data; the vertical line represents the Nyquist-wavenumber of the low-resolution grid

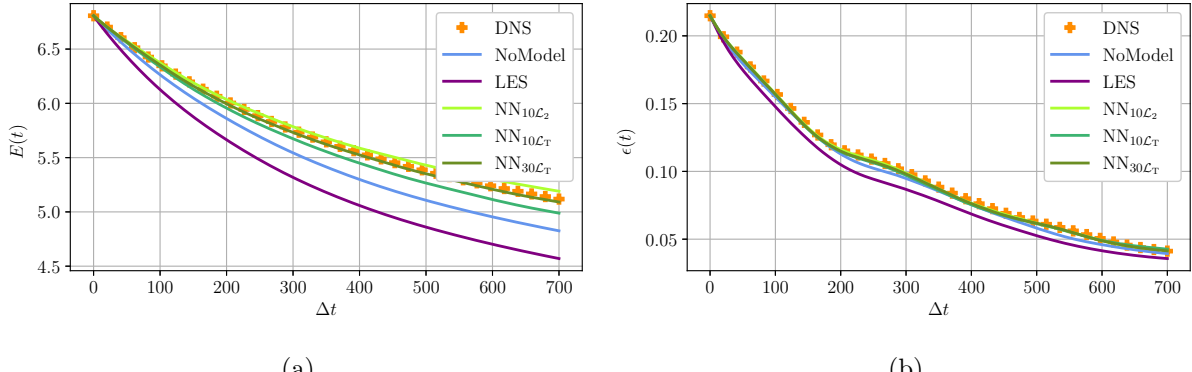


Figure 4: Comparison of DNS, no-model, LES, and learned model simulations with respect to resolved turbulence kinetic energy over time (a); and turbulence dissipation rate over time (b)

unrolled steps show the best performance at long simulation horizons. The higher total energy of the neural network modelled simulations can be attributed to the work done by the network forcing, which is visualised together with the SGS stress tensor work from the LES simulation as well as its SGS energy in figure 5. This analysis reveals that the neural networks do more work on the system as the LES model does, which explains the higher and more accurate turbulence energy in figure 4 and the spectral energy behavior at large scales in figure 3.

4 Temporally Developing Planar Mixing Layers

Next, we apply our method to the simulation of two-dimensional planar mixing layers. Due to their relevance to applications such as chemical mixing or combustion, mixing layers have been the focus of theoretical and numerical studies in the fluid-mechanics community. These studies have brought forth a large set and good understanding of *a-posteriori* evaluations, like the Reynolds-averaged turbulent statistics or the vorticity and momentum thickness. Herein, we use these evaluations to assess the accuracy of our learned models with respect to metrics that

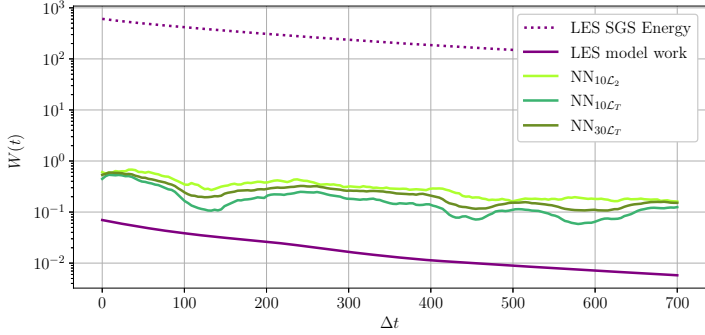


Figure 5: NN-model work on the flow field, work by the LES model and the estimated SGS energies from LES

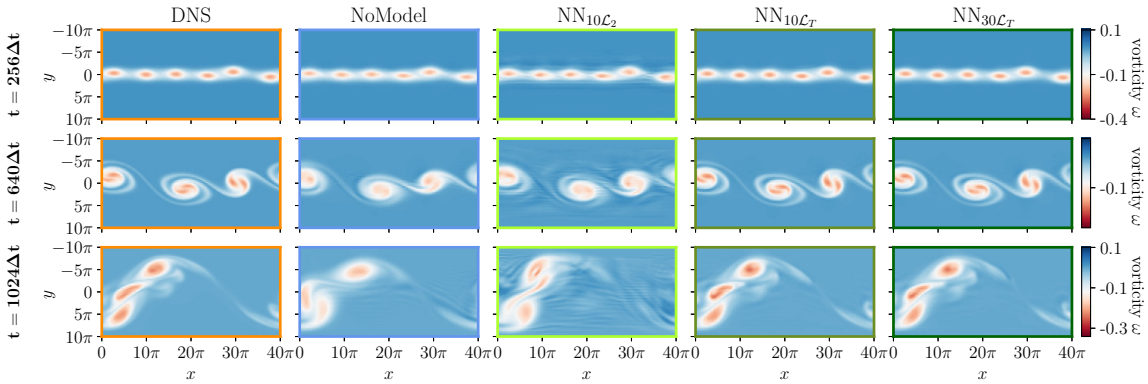


Figure 6: Vorticity visualisations of DNS, no-model, and learned model simulations at $t = (256, 640, 1024)\Delta t$ on the test dataset

are not directly part of the learning targets.

Temporally evolving planar mixing layers are the simplest numerical representation of a process driven by the Kelvin-Helmholtz instability in the shear layer. They are sufficiently defined by the Reynolds number, domain sizes, boundary conditions, and an initial condition. Aside from the shear layer represented by a tanh-profile, the initial flow fields feature an oscillatory disturbance that triggers the instability leading to the roll up of the shear layer. Numerous studies have focused on understanding the temporally evolving mixing layer, ranging from theoretical studies involving linear stability analysis [Michalke, 1964] to numerical simulation [Rogers and Moser, 1994]. Our setup is based on the work by Michalke [1964], who investigated the stability of the shear layer and proposed initialisations that lead to shear layer roll up. As initial condition, we add randomised modes to the mean profile, resulting in the stream-function

$$\Psi(x, y) = y + \frac{1}{2} \ln(1 + e^{-4y}) + a((\alpha y)^2 + 1)e^{-(\alpha y)^2} \cos(\omega_\Psi x), \quad (12)$$

where a is the amplitude of the perturbation, α parameterises the decay of the perturbation in y -direction, and ω_Ψ represents the perturbation frequency. The initial flow field can then be calculated by

$$u(x, y) = \frac{\partial \Psi}{\partial y}, \quad v(x, y) = -\frac{\partial \Psi}{\partial x}. \quad (13)$$

At the initial state this results in a velocity step $\Delta U = \frac{U_2}{U_1} = 1$ and a vorticity thickness of $\delta_\omega = \Delta U / \frac{\partial U}{\partial y}|_{\max} = 1$, where velocities marked as U represent mean-stream quantities. Thus, U_2 and U_1 are the fast and slow mean velocities of the shear layer. The computational domain of size

| | i | a_i | $\omega_{\Psi,i}$ |
|-------|-----|-------|-------------------|
| train | 1 | 6.0 | 0.7 |
| | 2 | 3.3 | 1.5 |
| test | 3 | 9.0 | 0.3 |

Table 2: Perturbation details for initial conditions of temporal mixing layer training and test datasets

| Name | Loss | Steps | MSE at t_e |
|--------------------|-----------------|-------|--------------|
| LR | - | - | 1.25e-3 |
| NN ₁₀ | \mathcal{L}_2 | 10 | 3.19e-4 |
| NN _{10,T} | \mathcal{L}_T | 10 | 3.31e-5 |
| NN _{30,T} | \mathcal{L}_T | 30 | 2.26e-5 |

Table 3: Training details for all trained models with the MSE evaluated w.r.t. DNS data at $t_e = 512\Delta t$

$(L_x, L_y) = (40\pi, 20\pi)$ is discretised by $(N_x, N_y) = (1024, 512)$ grid cells for the high-resolution dataset generation. The streamwise boundaries are periodic, while the spanwise boundaries in y -direction are set to a free-slip boundary where $\frac{\partial u}{\partial y}|_{\Omega_y} = 0$, $v|_{\Omega_y} = 0$ and $p|_{\Omega_y} = 0$. The Reynolds number based on the unperturbed mean profile and the vorticity thickness is calculated to be $Re = \frac{\Delta U \delta \omega}{\nu} = 250$ for all randomised initialisations. The simulations are run for $T = 420 = 12000\Delta t_{\text{DNS}}$. Our dataset consists of three simulations based on different initialisations. Their perturbation details are found in table 2. Two of these simulations were used as training datasets, while all of our evaluation is performed on the remaining one as test dataset.

Following the approach in section 3, the model training uses a $8 \times$ downscaling in space and time. The loss composition was set to $(\lambda_2, \lambda_E, \lambda_S, \lambda_{\text{MS}}) = (100, 2, 5 \times 10^{-2}, 0)$. We used the same CNN architecture as introduced earlier, though due to the difference in boundary conditions a different padding procedure was chosen (see appendix B). To illustrate the impact of the turbulence loss \mathcal{L}_T and an unrolling of 30 numerical steps, we compare to several variants with reduced loss formulations and fewer unrolling steps. Table 3 shows details of the model parameterisations.

The trained models were compared to a downsampled DNS and a no-model simulation, all sharing the same starting frame from the test-dataset. The resulting numerical solutions were compared at three different evolution times $t = [256 \ 640 \ 1024]\Delta t$. Figure 6 shows the vorticity heatmap of the solutions. Qualitatively, the simulations corrected by the CNN exhibit close visual proximity to the DNS by boosting peaks in vorticity where applicable, and additionally achieve a dampening of spurious oscillations.

These observations are matched by corresponding statistical evaluations. These statistics are obtained by averaging the simulation snapshots along their streamwise axis and the resulting turbulence fluctuations were processed for each evaluation time. Figure 7 shows that all trained models closely approximate the DNS reference with respect to their distribution of resolved turbulence kinetic energy and Reynolds stresses along the cross-section, while the no-model simulation clearly deviates. Note that the mixing process causes a transfer of momentum from fast to slow moving sections through the effects of turbulent fluctuations. The shear layer growth is thus dominated by turbulent diffusion. Consequently, accurate estimates of the turbulent fluctuations are necessary for the correct evolution of the mixing layer. These fluctuations are most visible in the Reynolds stresses $u'v'$, and an accurate estimation is an indicator for well modelled turbulent momentum diffusion. The evaluations also reveal that unrolling more timesteps during training gains additional performance improvements. These effects are most visible when comparing the 10-step and 30-step model in a long temporal evolution, as seen in the Reynolds stresses in figure 7. The evaluation of resolved turbulence kinetic energies shows that the models correct for the numerical dissipation of turbulent fluctuations, while, in contrast, there is an underestimation of kinetic energy in the no-model simulation.

The resolved turbulence kinetic energy spectra are evaluated to assess the spatial scales at which the corrective models are most active. The spectral analysis at the centerline is visualised in figure 8, whilst the kinetic energy obtained from fluctuations across the cross-section with respect

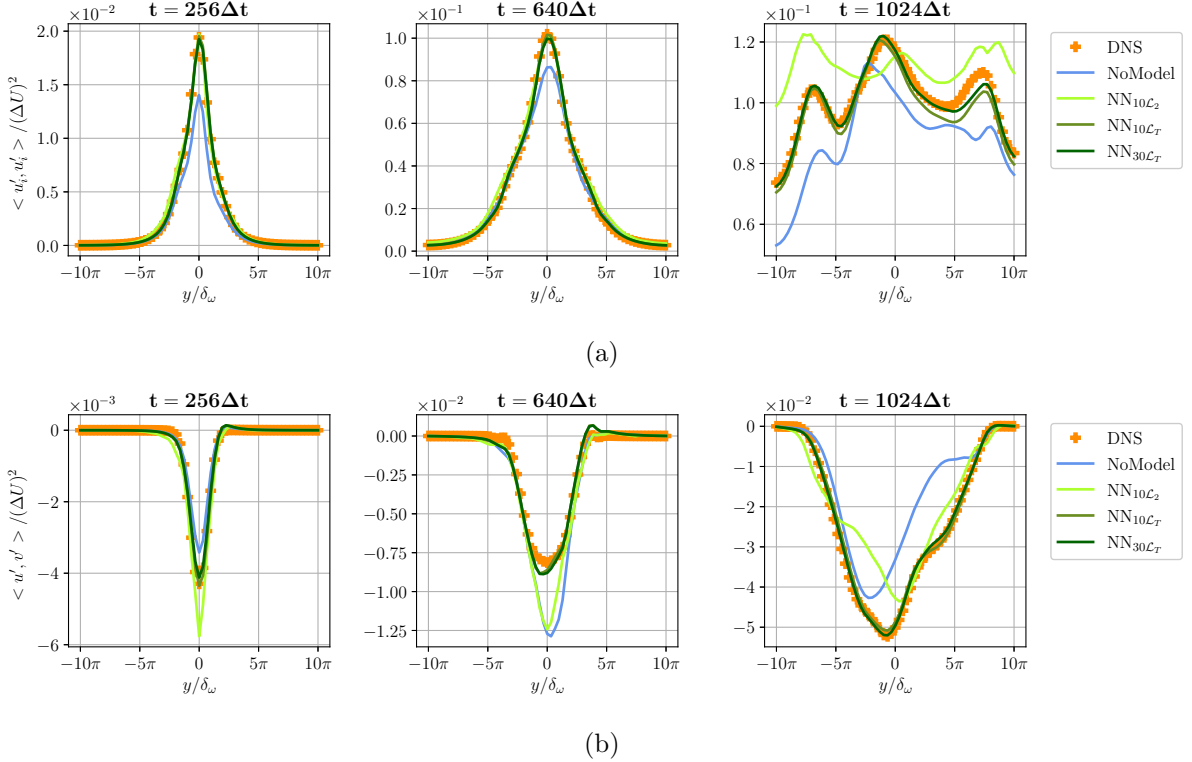


Figure 7: Comparison of DNS, no-model, and learned model simulations with respect to resolved turbulence kinetic energy (a), and Reynolds stresses (b)

to streamwise averages is shown in figure 9. These plots allow two main observations: Firstly, the deviation of kinetic energy mostly originates from medium-sized spatial scales, which are dissipated by the no-model simulation, but are accurately reconstructed by the neural network. This effect is connected to the dampening of vorticity peaks in the snapshots in figure 6. Secondly, the finest spatial scales of the no-model simulation seem to approximate the DNS in terms of kinetic energy. However, this behaviour can be attributed to numerical oscillations, which, as also seen in the snapshots in figure 6, exist for the no-model simulation but are missing in the modelled simulations. We thus conclude that the network learns to dampen numerical oscillations and reproduces physical fluctuations across all spatial scales.

It is worth noting that our method is capable of enhancing an under-resolved simulation across a wide range of turbulent motions. The vortex-size in the validation simulation ranges from $7\delta_{\omega_0}$ at the starting frame to $60\delta_{\omega_0}$ after evolving for $1200\Delta t$. This timespan encompasses two vortex merging events, both of which cannot be accurately reproduced with a no-model simulation, but are captured by the network models. This is shown in the comparison of the momentum thicknesses over time in figure 10. The reproduction of turbulence statistics (figure 7) yields, in the long term, an accurate turbulent diffusion of momentum and mixing layer growth.

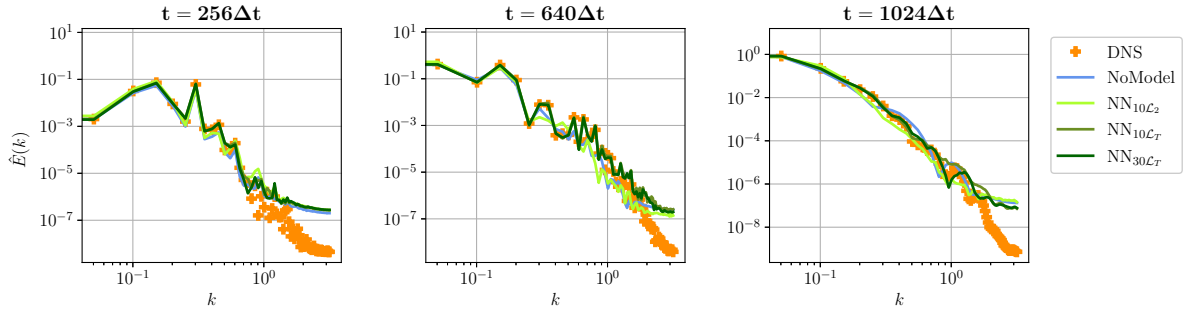


Figure 8: Centerline kinetic energy spectra for the downsampled DNS, no-model, and learned model simulations

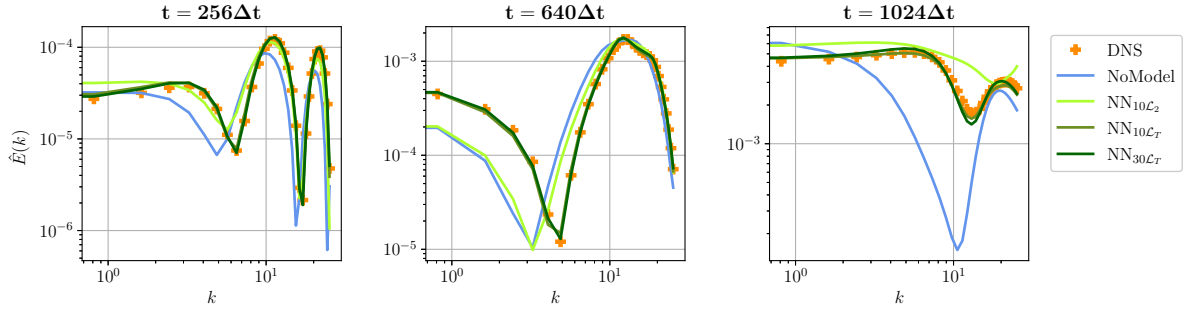


Figure 9: Cross-sectional kinetic energy spectra of the downsampled DNS, no-model, and learned model simulations

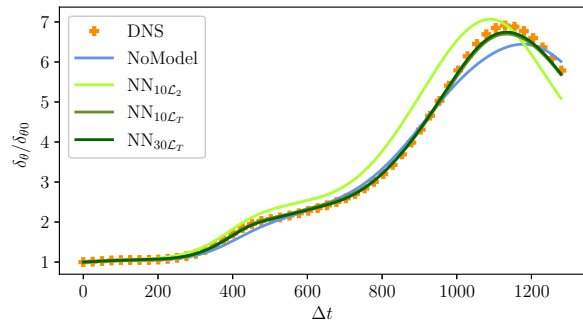


Figure 10: Momentum thickness of DNS, no-model, and learned model simulations, evaluated based on the streamwise averages

| | i | ϵ_i | n_i | ω_i |
|-------|-----|------------------------|----------|------------|
| 1 | 1 | 0.050 \bar{U} | .4 π | .22 |
| | 2 | 0.050 \bar{U} | .3 π | .11 |
| 2 | 1 | 0.075 \bar{U} | .3 π | .22 |
| | 2 | 0.025 \bar{U} | .3 π | .11 |
| train | 1 | 0.025 \bar{U} | .3 π | .22 |
| | 2 | 0.075 \bar{U} | .3 π | .11 |
| 3 | 1 | 0.060 \bar{U} | .3 π | .22 |
| | 2 | 0.040 \bar{U} | .3 π | .11 |
| 4 | 1 | 0.040 \bar{U} | .3 π | .22 |
| | 2 | 0.060 \bar{U} | .3 π | .11 |
| test | 1 | 0.082 \bar{U} | .4 π | .22 |
| | 2 | 0.018 \bar{U} | .3 π | .11 |

Table 4: Perturbation details for the inlet condition of training and test datasets

5 Spatially Developing Planar Mixing Layers

In contrast to the temporally developing mixing layers investigated in section 4, the spatially developing counterpart features a fixed view on a quasi-steady flow field, which introduces a new set of challenges to the learning task. While the main difficulty in previous transient simulations was the modelling of an evolving range of turbulent scales, the quasi-steady nature of the spatially developing mixing layer requires a reproduction of the turbulent statistics in its own statistically steady state. This in turn necessitates long-term accuracy and stability.

Spatially mixing layers develop from an instability in the shear layer. This instability is driven by a disturbance at the inlet, whose characteristics have great effect on the mixing layer growth [Ho and Huang, 1982]. In a simulation environment, these disturbances are realised by a Dirichlet inlet boundary condition, where temporally varying perturbations are added to a steady mean flow profile. As proposed by Ko et al. [2008], a suitable inlet condition including perturbations can be written as

$$u_{in}(y, t) = 1 + \frac{\Delta U}{2} \tanh(2y) + \sum_{i=1}^{N_i} \epsilon_i (1 - \tanh^2(y/2)) \cos(n_i y) \sin(\omega_i t), \quad (14)$$

where $N_i = 2$ holds for our simulations. Furthermore, we used inviscid wall conditions for the two y -normal spanwise boundaries, and the outflow boundary was realised by a simple Neumann condition with a stabilising upstream sponge layer. For all simulations, we set the characteristic velocity ratio $\Delta U = 1$ and the vorticity thickness to $\delta_\omega = 1$. The vorticity-thickness Reynolds number is set to $Re_{\delta_\omega} = \frac{\Delta U \delta_\omega}{\nu} = 500$. To generate the DNS dataset, this setup was discretised by a uniform grid with $(N_x, N_y) = (2048, 512)$ resolving the domain of size $(L_x, L_y) = (256, 64)$. The timesteps were chosen such that $CFL = 0.3$ and the temporal evolution was run for 7 periods of the slowest perturbation mode $i = 2$ to reach a statistically steady state, before subsequent frames were entered into the dataset. A further 28 periods of the slowest perturbation mode were simulated to generate 32000 samples of the quasi-steady state. The training dataset consists of 5 such simulations with different perturbations, as summarised in table 4. A downsampling ratio of $8 \times$ was again chosen for the learning setup. The input to the network was set to include only the main simulation frame without the sponge layer region.

Our best performing model applied the turbulence loss \mathcal{L}_T , with the loss factors set to $(\lambda_2, \lambda_E, \lambda_S, \lambda_{MS}) = (50, 0.5, 2, 0.5)$, and an unrollment of 60 solver steps. The timespan

| Name | Loss | Steps | MSE at t_e |
|---------------------|-----------------|-------|--------------|
| LR | - | - | 3.14e-2 |
| NN _{10,LT} | \mathcal{L}_T | 10 | 5.41e-3 |
| NN _{30,LT} | \mathcal{L}_T | 30 | 3.05e-3 |
| NN _{60,LT} | \mathcal{L}_T | 60 | 1.69e-3 |

Table 5: Model details for all trained models with the MSE evaluated with respect to DNS from test-data at $t_e = 1000\Delta t$

covered by these 60 solver steps is comparable to a full period of the slowest perturbation mode. We will cover the relevance of this relation in a later evaluation. Our 60-step model was also trained differently by stopping the backpropagation gradient every 20 steps. This divides one training iteration into three subsections, for which optimisation gradients were calculated individually and then aggregated. We designed this training procedure to avoid common pitfalls of optimising through recurring network applications, like exploding or diminishing gradients. Once again, we show comparisons with additional setups, the parametric details of which can be found in table 5. It shows that the simulation with the 30-step neural network outperforms the no-model baseline by almost an order of magnitude. For these evaluations, we assessed the model capabilities by running a CNN-corrected forward simulation. This simulation was initialised with a downsampled frame from the DNS test dataset in its fully-developed state. The instability in this simulation was then driven by the same inlet perturbations as present in the DNS test case. The simulation was run for $2500\Delta t$, or 18 periods of the slowest perturbation mode in order to obtain data from a statistically stable state. Despite this time frame being orders of magnitude longer than what is seen by the models at training time, the 60-step model retains a stable simulation that closely matches the behavior of the DNS reference. Interestingly, this longer unrollment is crucial to arrive at a stable model. The models trained with shorter unrollment exhibit various degrees of spurious oscillations, most likely due to the fact that they see more and more self-excited simulation states. As before, we omit purely data-driven models trained with pre-computed simulation states. These produce undesirable solutions within a few time steps of simulating the test cases. The vorticity visualisations after half a period of the slowest perturbation mode ($70\Delta t$) and after 4 periods or one flow through time ($600\Delta t$) are shown in figure 11a and figure 11b, and compared to DNS and the no-model simulation. The early evaluation in figure 11a reveals a severe loss of detail in the no-model simulation, even after a short time horizon. Over this time-span, the learned model achieves a close visual reproduction. Additionally, the later evaluation in figure 11b shows a delayed roll-up in the no-model simulation, whereas the learned model maintains the roll-up location and shows improved accuracy. This behaviour is clarified by the Reynolds-averaged properties of the simulations, for which resolved Reynolds stresses and turbulence kinetic energies were calculated on the basis of the respective statistically steady simulations. As shown in figure 12, the no-model statistics severely deviate from the targeted DNS. In contrast, the corrective forcing inferred by the trained models approximates these statistics more accurately. The delayed roll-up of the no-model simulation and the improvement of the modelled ones is connected to the Reynolds stresses. The Reynolds stresses indicate turbulent diffusion of momentum, and figure 12 shows that the CNN learned to encourage turbulent fluctuations at the start of the mixing layer. The fluctuations trigger the shear layer instability and feed the roll-up, with decisive implications for the downstream development of the mixing layer. Especially the long unrollment of 60 steps benefits the model performance. Our testing revealed that the large performance improvement of this model only materialised when the unrollment was split into subsections divided by gradient stopping, as described earlier.

These observations regarding the Reynolds stresses extend to the resolved turbulence kinetic energies (figure 12), where the same turbulent fluctuations yield an accurate reproduction of the DNS. The learned models are not limited to a specific spatial scale, but precisely match the DNS on all turbulent scales when comparing the center-line kinetic energy spectra in figure 13.

Nevertheless, the model accuracy slightly deteriorates further downstream from the initial roll-up location. This is best captured by the evaluations of vorticity and momentum thickness in figures 14a and 14b. These plots show that the learned model simulations feature a delayed development of the mixing layer immediately after the first roll-up, which results in a downstream-shift of these quantities. According to these metrics, the 60-step model is best at recovering the DNS behaviour further downstream. Consequently, the evaluation of Reynolds stresses at $x = 192\Delta x$ (figure 12) shows large discrepancies between DNS and learned model

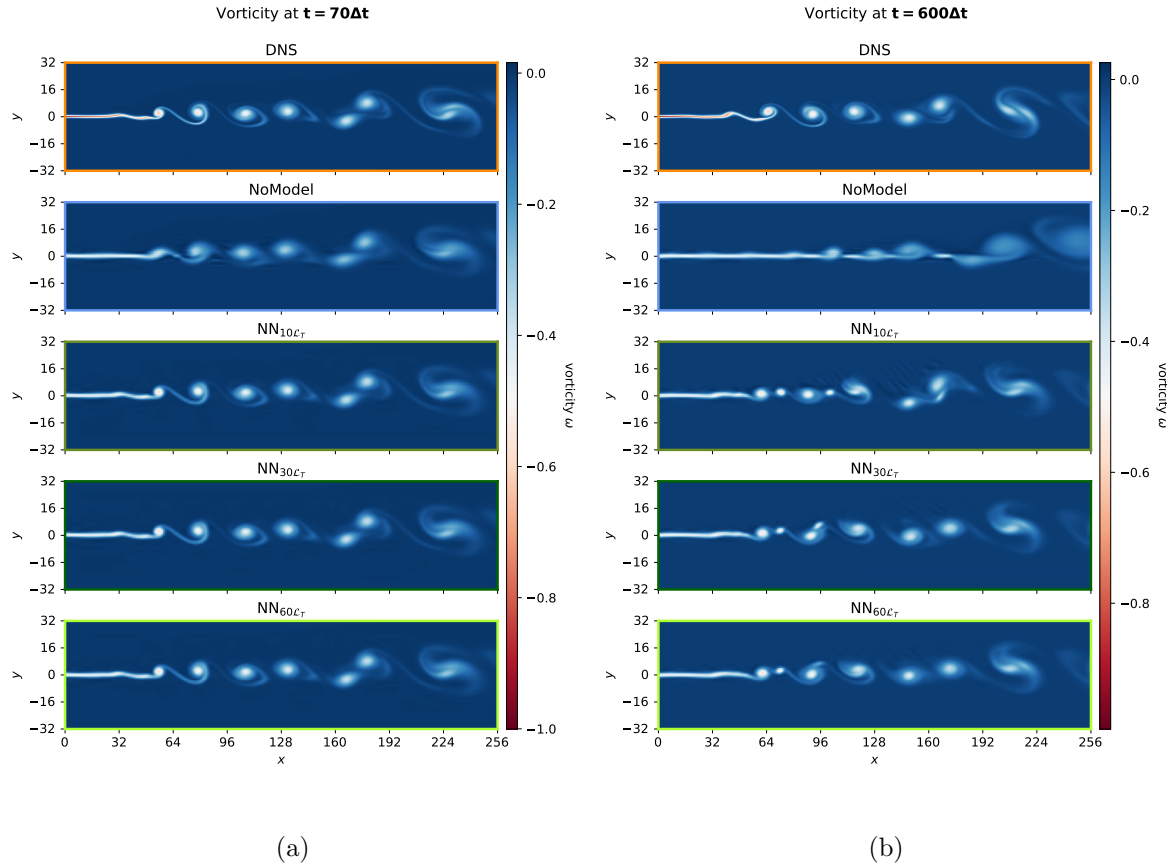


Figure 11: Vorticity heatmaps of the spatial mixing layer simulations at (a) $t = 70\Delta t$, and (b) $t = 600\Delta t$, on the test dataset

simulation for all but the 60-step model. For the remaining learned models, this behaviour can be attributed to the shifted location of vortex merging. Note however, that despite not being capable of exactly reproducing the entire mixing layer up to the finest detail, the learned model still greatly outperforms a no-model simulation.

Additionally, the evaluations show the benefits of training through multiple unrolled steps. The 10-step model develops instabilities after $500\Delta t$, which is equivalent to one flow-through time. From this time on, the learned model only sees self-excited instabilities in the mixing layer. In this extrapolation case on the test dataset, this causes spurious oscillations and thus a deterioration of solution quality. The 30-step model shows this behaviour to a lesser extent and generates a stable, quasi-steady progression of the mixing layer for this case of temporal extrapolation. Even better behaviour is only achieved by the 60-step model by practically eliminating the instabilities seen in other models.

While previous evaluations showcased the stability improvements gained by training through multiple solver steps, another benefit of this approach relates to the temporal fluctuations in DNS training data. As visualised in figure 15, only some of the interactions between CNN and these temporal oscillations are covered in a training iteration. Consequently, the training loop imposes a high-pass cutoff on the observed frequencies that directly depends on the number of unrolled solver steps. To extract the temporal features that our models learned from the training dataset, we calculate the power-spectral density of the velocity fields at sampling point $(x, y) = (160, 0)$ on training data. The sampling time-span for the learned models starts after one flow-through time and stops after the next 4 flow-through times passed. The resulting power-spectral densities are compared to a long-term evaluation of the DNS data, and a relative error between the

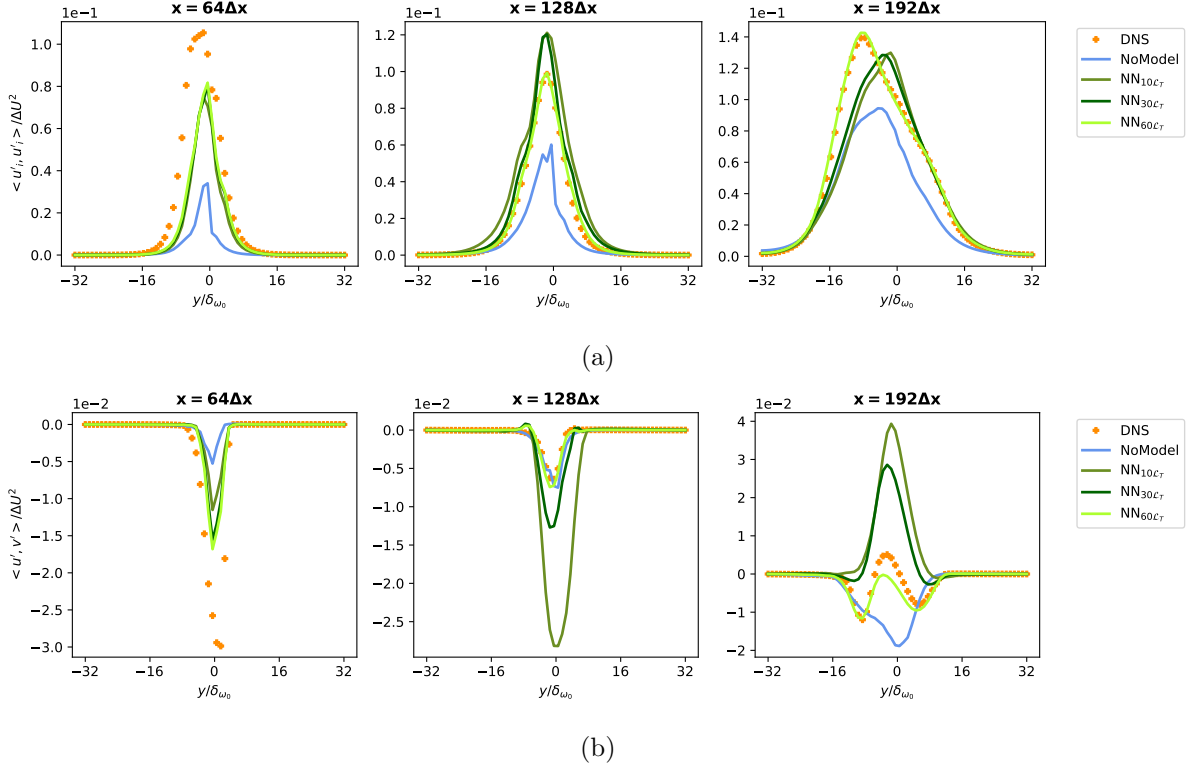


Figure 12: Comparison of downsampled DNS, no-model, and learned model simulations with respect to Reynolds-averaged resolved turbulence kinetic energy (a); and Reynolds stresses (b)

spectra is computed. The results are shown in figure 15 and support the following observations. Firstly, all learned models can capture the discrete nature of the dominant frequencies quite well. Especially the 60-step model shows good approximation of the DNS evaluation. In contrast, the no-model does not match the DNS characteristics. Secondly, the relative error of the power spectra generated by the 60-step model is substantially lower for all but the finest frequencies. Since 30- and 10-step models only saw the interaction with fine scales during their training, these models perform worse on the lower frequencies, which results in higher relative errors for the relatively low roll-up and merging frequencies.

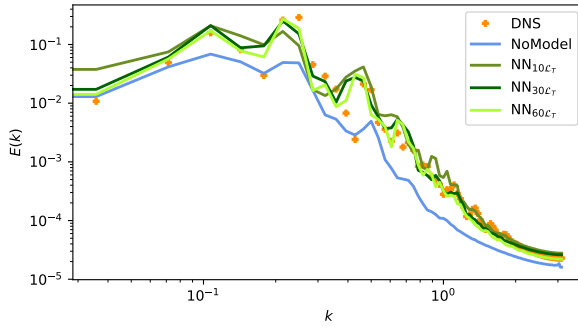


Figure 13: Centerline kinetic energy spectra for downsampled DNS, no-model, and learned model simulations

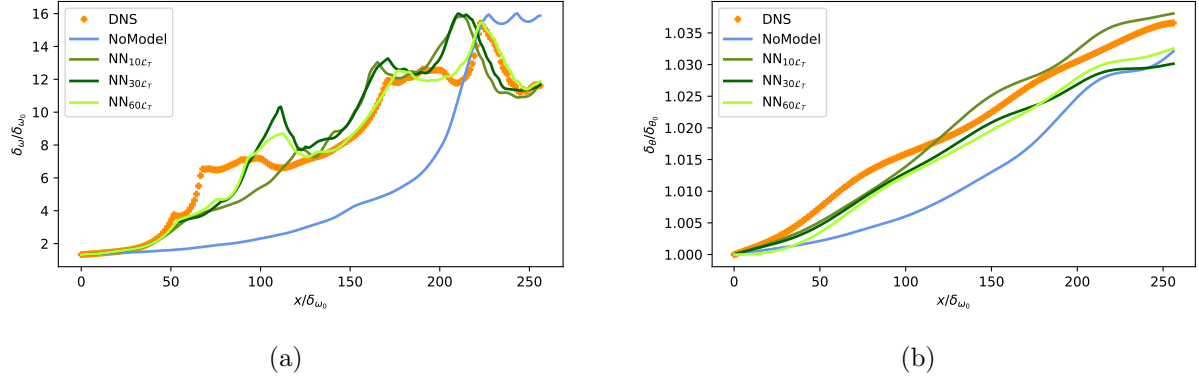


Figure 14: Vorticity and momentum thickness of the downsampled DNS, no-model, and learned model simulations

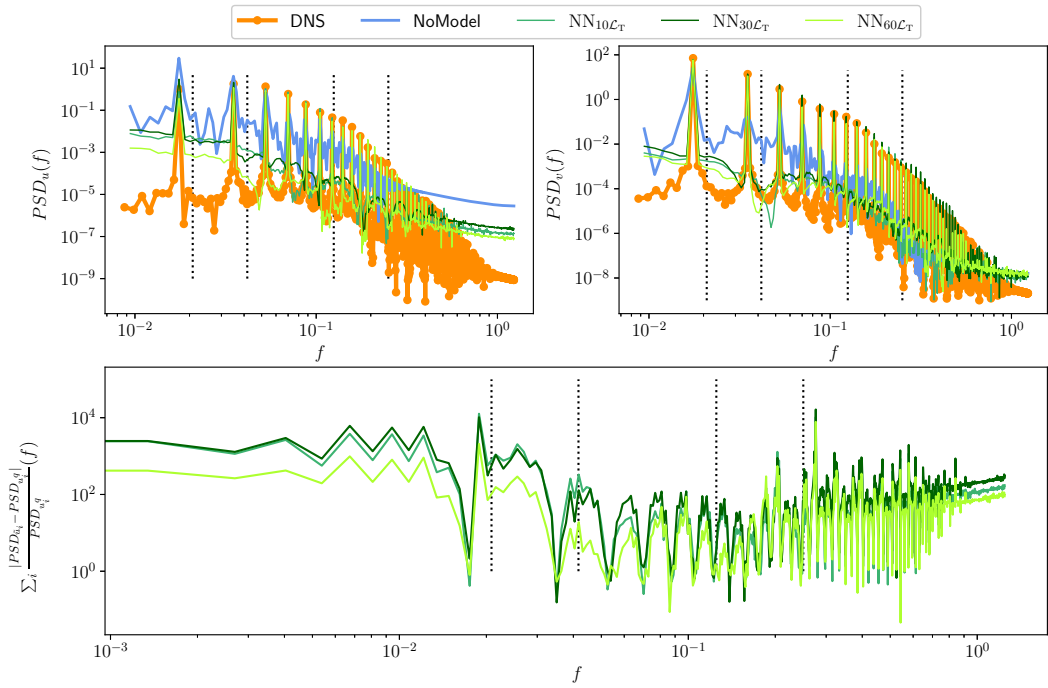


Figure 15: Power Spectral Density of velocity fluctuations over time at sampling point $(x, y) = (192\Delta x, 0)$ based on the training dataset for DNS, no-model and learned model simulations at top; bottom figure displays the relative error of the power densities over frequencies, accumulated for both velocity components; frequencies to the right of a dotted vertical line are fully enclosed in a training iteration; vertical lines correspond to (60, 30, 10, 5) unrolled steps from left to right

| | Name | Resolution | Time until t_e | # of Δt | Time per Δt | MSE |
|-----|---------|--------------------|------------------|-----------------|---------------------|-----------|
| IDT | DNS | 1024×1024 | $14497.7s$ | 8000 | $1.812 \pm 0.432s$ | 0 |
| | NN | 128×128 | $71.2s$ | 1000 | $0.071 \pm 0.015s$ | $1.96e-2$ |
| | NoModel | 128×128 | $65.5s$ | 1000 | $0.066 \pm 0.066s$ | $5.45e-2$ |
| | - | 256×256 | $240.6s$ | 2000 | $0.120 \pm 0.027s$ | $1.07e-2$ |
| | - | 512×512 | $1348.8s$ | 4000 | $0.337 \pm 0.049s$ | $1.03e-3$ |
| TML | DNS | 1024×512 | $12467.8s$ | 8000 | $1.559 \pm 0.764s$ | 0 |
| | NN | 128×64 | $149.4s$ | 500 | $0.150 \pm 0.053s$ | $1.90e-5$ |
| | NoModel | 128×64 | $144.5s$ | 500 | $0.145 \pm 0.052s$ | $1.23e-3$ |
| | - | 256×128 | $593.5s$ | 2000 | $0.297 \pm 0.148s$ | $2.30e-4$ |
| | - | 340×170 | $1054.0s$ | 2656 | $0.395 \pm 0.216s$ | $1.07e-4$ |
| SML | - | 512×256 | $2154.9s$ | 4000 | $0.539 \pm 0.259s$ | $2.51e-5$ |
| | DNS | 2048×512 | $81925.3s$ | 8000 | $10.242 \pm 1.144s$ | 0 |
| | NN | 256×64 | $1835.7s$ | 1000 | $1.838 \pm 0.258s$ | $1.69e-3$ |
| | NoModel | 256×64 | $1815.4s$ | 1000 | $1.817 \pm 0.450s$ | $2.03e-2$ |
| | - | 512×128 | $3971.3s$ | 2000 | $1.987 \pm 0.348s$ | $6.22e-3$ |
| | - | 768×192 | $6719.23s$ | 2667 | $2.240 \pm 0.273s$ | $7.57e-4$ |
| | - | 1024×256 | $12071.5s$ | 4000 | $3.019 \pm 0.245s$ | $3.13e-4$ |

Table 6: Computational performance comparison over $t_e = 1000\Delta t$ for the used flow scenarios, Isotropic Decaying Turbulence (IDT), Temporal Mixing Layer (TML) and Spatial Mixing Layer (SML); MSE values are evaluated on the velocity field at $500\Delta t$

6 Computational Performance

The development of turbulence models is ultimately motivated by a reduced computational cost, which facilitates numerical simulations in flow scenarios where a DNS is prohibitively expensive. Preceding sections have outlined the corrective capabilities of our learned models. We now seek to put these improvements into perspective by studying the computational cost of our learned models at inference time. For all of our performance evaluations, an *Intel Xeon E5-1650* CPU and a *Nvidia GTX 1080Ti* GPU are used. We use the computational setups from our model evaluation runs on test data in the Isotropic Turbulence, Temporal Mixing Layer and Spatial Mixing Layer cases in sections 3, 4 and 5 respectively. Exactly as before, an $8\times$ scaling factor is deployed on both the spatial resolution and timestep size. We then run the simulations until the time $t_e = 1000\Delta t$ is reached, while recording the required computational time for each timestep. The results are summarised in table 6, where the total simulation time as well as per-timestep values are listed. We also assess the computational cost of a no-model simulation that matches the performance of our models. The resulting data shows that the neural network incurs only a negligible cost of circa 10% in comparison to no-model simulations at the same resolution. The learned models clearly outperform the no-model variants in terms of MSEs, and incur only a fraction of the computational cost required for the DNS variants.

In addition, we provide the temporal evolution of the MSE evaluated on resolved turbulence kinetic energies for all three scenarios in figure 16. From this evaluation, we conclude that our method consistently outperforms simulations with a $2\times$ higher resolution in spatial and temporal dimensions. Additionally, we found our learned models to often be on-par with $4\times$ higher resolved simulations, e.g. in the first half of the temporal mixing layer case. On the basis of the clock-times from table 6, this corresponds to a speedup of 3.3 over $2\times$ isotropic turbulence simulations. For the mixing layer cases, the hybrid model is on average resembling the performance of $3\times$ reference simulations, which corresponds to a speed-up of 7.0 for the temporal, and 3.7 for the spatial mixing layer. For the former, our model even closely matches the performance of a $4\times$ simulation for several hundred time steps, which represents a speedup of 14.4.

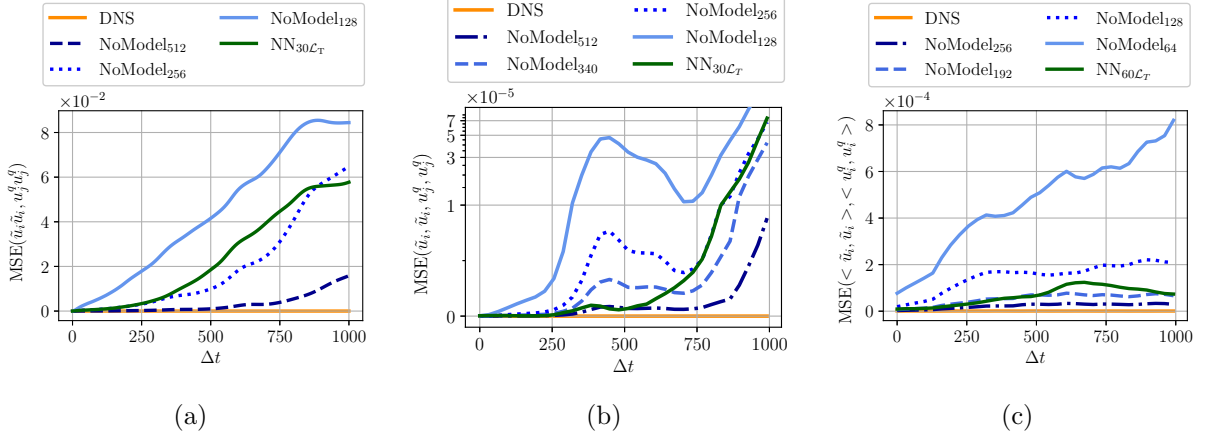


Figure 16: Similarity evolutions over time measured by the MSE on resolved turbulence kinetic energy for randomised turbulence simulations (a), temporal mixing layer simulations (b), and spatial mixing layer simulations (c)

While other works have reported even larger performance improvements [Kochkov et al., 2021], we believe that our measurements are representative of real-world scenarios with higher-order solvers. Asymptotically, we also expect even larger payoffs for the high-resolution, three-dimensional simulations that are prevalent in real-world applications.

Naturally, the training of each neural network requires a substantial one-time cost. In our case, the networks for the spatial mixing layer case required training for 4 to 6 days on a single GPU for the 10-step and 60-step models, respectively. However, under the assumption that the learned turbulence model can be employed in a larger number of simulations to produce new outputs, this cost will quickly amortise.

7 Conclusion

In this paper, we introduced a hybrid method to integrate neural networks in a numerical solver in order to model the finest turbulent scales when these cannot be resolved by the simulation grid. The differentiable nature of our implementation of the PISO solver allows us to train the network through multiple unrolled steps. We deem this feature crucial, since we found a strong dependence of the model performance and long-term stability on the number of unrolled steps. We showcased the application of our method to three different flow scenarios, the two-dimensional isotropic decaying turbulence, the temporally developing mixing layer and the spatially developing mixing layer, whilst keeping the network architecture identical. The optimisation of network parameters yielded good results when optimising towards the \mathcal{L}_2 -loss, but could be substantially improved through our formulation of the turbulence loss \mathcal{L}_T .

When run in inference mode, the simulation based on the learned models trained with our method remained stable for long periods and allowed us to run simulations vastly surpassing the initial training horizon. Our models proved to be in good agreement with the DNS test datasets when compared on the basis of *a-posteriori* statistics. These agreements were obtained despite the fact that the evaluation metrics were not a target of the training optimisation, and that the test datasets constitute an extrapolation from training data. Furthermore, our hybrid approach achieved good results on a wide range of scales, with the Reynolds number varying from $Re = 126$ to $Re = 296$ in the isotropic turbulence case, and the vortex sizes ranging from $7\delta_{\omega_0}$ to $60\delta_{\omega_0}$ in the temporal mixing layer. Similarly, our approach yielded a learned model simulation that remained accurate and stable in a quasi-steady test-case of the spatial mixing layer. These spatial mixing layer models were trained with a range of perturbation parameters

and proved good extrapolation accuracy towards this quantity. In our test-cases, the learned model simulation accurately reproduced the turbulence kinetic energy in its spectral distribution as well as its temporal evolution. Furthermore, the learned models captured the turbulent fluctuations, which lead to a precise modelling of vortex roll-up and merging events. Our results also demonstrate the importance of unrolling simulator steps during training in achieving high accuracy and stability. Such models are effectively trained by our approach of optimising all sub-ranges of a multi-step training loop divided by gradient stopping. This approach differs from the common practice in machine learning, where early evaluations of the neural network are usually discarded when gradient stopping is applied. Our learned models provides a significant increase in computational performance, where speedups in terms of computation time of a factor of up to 14 are observed. The additional resources required for model inference are minor and can be justified with the gains in the solution accuracy.

In its current form, our method has several limitations, such as the initial one time cost to train the neural network turbulence model. Also, our tests have focused on regular, Cartesian grids. However, more flexible convolutions [Sanchez-Gonzalez et al., 2020; Ummenhofer et al., 2019] could be employed to use our method on more flexible mesh structures with irregular discretisations. Moreover, even regular CNNs can be extended to take regular, non-uniform and stretched meshes into account [Chen and Thuerey, 2021]. For instance, this is highly important for wall-bounded flows and fluid-structure interactions. Similarly, further interesting extensions could work towards a differentiable solver that directly trains towards a-posteriori statistics, or study the modelling capabilities of different network architectures with respect to the modelled turbulent scales.

To summarize, the improvements in accuracy and runtime of our approach render the proposed combination of neural network and numerical solver suitable for a variety of settings. As the ground truth data is not restricted to originate from the same solver architecture, it could stem from different numerical schemes such as higher order spectral methods. Furthermore, the learned models could offer significant savings when a large quantity of turbulent simulations is required. This is especially important for inverse problems such as flow optimisation tasks. Due to the super-linear scaling of existing solvers, our method also has the potential to provide even greater performance benefits when applied to three dimensional flow fields.

Funding This work was supported by European Research Council (ERC) Consolidator Grant CoG-2019-863850 (SpaTe).

Declaration of interests The authors report no conflict of interests.

Further information <https://github.com/tum-pbs/differentiable-piso>

References

Martín Abadi, Paul Barham, Jianmin Chen, Zhifeng Chen, Andy Davis, Jeffrey Dean, Matthieu Devin, Sanjay Ghemawat, Geoffrey Irving, Michael Isard, et al. Tensorflow: A system for large-scale machine learning. In *12th USENIX symposium on operating systems design and implementation (OSDI 16)*, pages 265–283, 2016.

Vadym Aizinger, Peter Korn, Marco Giorgetta, and Sebastian Reich. Large-scale turbulence modelling via α -regularisation for atmospheric simulations. *Journal of Turbulence*, 16(4):367–391, 2015.

Saad Albawi, Tareq Abed Mohammed, and Saad Al-Zawi. Understanding of a convolutional neural network. In *2017 International Conference on Engineering and Technology (ICET)*, pages 1–6. Ieee, 2017.

Christos D Argyropoulos and NC Markatos. Recent advances on the numerical modelling of turbulent flows. *Applied Mathematical Modelling*, 39(2):693–732, 2015.

Iain Edward Barton. Comparison of simple-and piso-type algorithms for transient flows. *International Journal for numerical methods in fluids*, 26(4):459–483, 1998.

Andrea Beck, David Flad, and Claus-Dieter Munz. Deep neural networks for data-driven les closure models. *Journal of Computational Physics*, 398:108910, 2019.

Saakaar Bhatnagar, Yaser Afshar, Shaowu Pan, Karthik Duraisamy, and Shailendra Kaushik. Prediction of aerodynamic flow fields using convolutional neural networks. *Computational Mechanics*, 64(2):525–545, 2019.

Silvia Bozzi, Davide Dominissini, Alberto Redaelli, and Giuseppe Passoni. The effect of turbulence modelling on the assessment of platelet activation. *Journal of Biomechanics*, 128:110704, 2021.

JR Chasnov. On the decay of two-dimensional homogeneous turbulence. *Physics of Fluids*, 9(1):171–180, 1997.

Li-Wei Chen and Nils Thuerey. Towards high-accuracy deep learning inference of compressible turbulent flows over aerofoils. In *arXiv*, 2021.

Yu Cheng, Marco Giometto, Pit Kauffmann, Ling Lin, Chen Cao, Cody Zupnick, Harold Li, Qi Li, Ryan Abernathey, and Pierre Gentine. Deep learning for subgrid-scale turbulence modeling in large-eddy simulations of the atmospheric boundary layer. *arXiv preprint arXiv:1910.12125*, 2019.

Haecheon Choi and Parviz Moin. Grid-point requirements for large eddy simulation: Chapman’s estimates revisited. *Physics of fluids*, 24(1):011702, 2012.

Filipe de Avila Belbute-Peres, Kevin Smith, Kelsey Allen, Josh Tenenbaum, and J Zico Kolter. End-to-end differentiable physics for learning and control. *Advances in neural information processing systems*, 31:7178–7189, 2018.

Karthik Duraisamy, Gianluca Iaccarino, and Heng Xiao. Turbulence modeling in the age of data. *Annual Review of Fluid Mechanics*, 51:357–377, 2019.

Michael B Giles, Mihai C Duta, Jens-Dominik Muller, and Niles A Pierce. Algorithm developments for discrete adjoint methods. *AIAA journal*, 41(2):198–205, 2003.

Luca Guastoni, Alejandro Güemes, Andrea Ianiro, Stefano Discetti, Philipp Schlatter, Hossein Azizpour, and Ricardo Vinuesa. Convolutional-network models to predict wall-bounded turbulence from wall quantities. *Journal of Fluid Mechanics*, 928, 2021.

Chih-Ming Ho and Lein-Saing Huang. Subharmonics and vortex merging in mixing layers. *Journal of Fluid Mechanics*, 119:443–473, 1982.

Philipp Holl, Nils Thuerey, and Vladlen Koltun. Learning to control pdes with differentiable physics. In *International Conference on Learning Representations*, 2020.

Raad I Issa. Solution of the implicitly discretised fluid flow equations by operator-splitting. *Journal of computational physics*, 62(1):40–65, 1986.

S-W Kim and TJ Benson. Comparison of the smac, piso and iterative time-advancing schemes for unsteady flows. *Computers & fluids*, 21(3):435–454, 1992.

Jordan Ko, Didier Lucor, and Pierre Sagaut. Sensitivity of two-dimensional spatially developing mixing layers with respect to uncertain inflow conditions. *Physics of Fluids*, 20(7):077102, 2008.

Dmitrii Kochkov, Jamie A Smith, Ayya Alieva, Qing Wang, Michael P Brenner, and Stephan Hoyer. Machine learning–accelerated computational fluid dynamics. *Proceedings of the National Academy of Sciences*, 118(21), 2021.

Corentin J Lapeyre, Antony Misdariis, Nicolas Cazard, Denis Veynante, and Thierry Poinsot. Training convolutional neural networks to estimate turbulent sub-grid scale reaction rates. *Combustion and Flame*, 203:255–264, 2019.

DK Lilly. Numerical simulation of developing and decaying two-dimensional turbulence. *Journal of Fluid Mechanics*, 45(2):395–415, 1971.

Wenjie Luo, Yujia Li, Raquel Urtasun, and Richard Zemel. Understanding the effective receptive field in deep convolutional neural networks. In *Proceedings of the 30th International Conference on Neural Information Processing Systems*, pages 4905–4913, 2016.

Jonathan F MacArt, Justin Sirignano, and Jonathan B Freund. Embedded training of neural-network subgrid-scale turbulence models. *Physical Review Fluids*, 6(5):050502, 2021.

Romit Maulik, Omer San, Adil Rasheed, and Prakash Vedula. Subgrid modelling for two-dimensional turbulence using neural networks. *Journal of Fluid Mechanics*, 858:122–144, 2019.

Alfons Michalke. On the inviscid instability of the hyperbolictangent velocity profile. *Journal of Fluid Mechanics*, 19(4):543–556, 1964.

Guido Novati, Hugues Lascombes de Laroussilhe, and Petros Koumoutsakos. Automating turbulence modelling by multi-agent reinforcement learning. *Nature Machine Intelligence*, 3(1):87–96, 2021.

Jonghwan Park and Haecheon Choi. Toward neural-network-based large eddy simulation: application to turbulent channel flow. *Journal of Fluid Mechanics*, 914, 2021.

Stephen B Pope. *Turbulent Flows*. Cambridge university press, 2000.

Stephen B Pope. Ten questions concerning the large-eddy simulation of turbulent flows. *New journal of Physics*, 6(1):35, 2004.

Michael M Rogers and Robert D Moser. Direct simulation of a self-similar turbulent mixing layer. *Physics of Fluids*, 6(2):903–923, 1994.

Omer San. A dynamic eddy-viscosity closure model for large eddy simulations of two-dimensional decaying turbulence. *International Journal of Computational Fluid Dynamics*, 28(6-10):363–382, 2014.

Omer San and Anne E Staples. High-order methods for decaying two-dimensional homogeneous isotropic turbulence. *Computers & Fluids*, 63:105–127, 2012.

Alvaro Sanchez-Gonzalez, Jonathan Godwin, Tobias Pfaff, Rex Ying, Jure Leskovec, and Peter Battaglia. Learning to simulate complex physics with graph networks. In *International Conference on Machine Learning*, pages 8459–8468. PMLR, 2020.

Fabrizio Sarghini, G De Felice, and Stefania Santini. Neural networks based subgrid scale modeling in large eddy simulations. *Computers & fluids*, 32(1):97–108, 2003.

Justin Sirignano, Jonathan F MacArt, and Jonathan B Freund. Dpm: A deep learning pde augmentation method with application to large-eddy simulation. *Journal of Computational Physics*, 423:109811, 2020.

Jeffrey P Slotnick, Abdollah Khodadoust, Juan Alonso, David Darmofal, William Gropp, Elizabeth Lurie, and Dimitri J Mavriplis. Cfd vision 2030 study: a path to revolutionary computational aerosciences. Technical report, 2014.

Nils Thuerey, Konstantin Weißenow, Lukas Prantl, and Xiangyu Hu. Deep learning methods for reynolds-averaged navier–stokes simulations of airfoil flows. *AIAA Journal*, 58(1):25–36, 2020.

Nils Thuerey, Philipp Holl, Maximilian Mueller, Patrick Schnell, Felix Trost, and Kiwon Um. Physics-based deep learning. *arXiv preprint arXiv:2109.05237*, 2021.

Kiwon Um, Robert Brand, Yun Fei, Philipp Holl, and Nils Thuerey. Solver-in-the-loop: Learning from differentiable physics to interact with iterative pde-solvers. In *Advances in Neural Information Processing Systems*, 2020.

Benjamin Ummenhofer, Lukas Prantl, Nils Thuerey, and Vladlen Koltun. Lagrangian fluid simulation with continuous convolutions. In *International Conference on Learning Representations*, 2019.

Chenyue Xie, Ke Li, Chao Ma, and Jianchun Wang. Modeling subgrid-scale force and divergence of heat flux of compressible isotropic turbulence by artificial neural network. *Physical Review Fluids*, 4(10):104605, 2019.

Chenyue Xie, Jianchun Wang, Hui Li, Minping Wan, and Shiyi Chen. Spatially multi-scale artificial neural network model for large eddy simulation of compressible isotropic turbulence. *AIP Advances*, 10(1):015044, 2020.

Zhiyin Yang. Large-eddy simulation: Past, present and the future. *Chinese journal of Aeronautics*, 28(1):11–24, 2015.

Xin Yu, Basura Fernando, Richard Hartley, and Fatih Porikli. Super-resolving very low-resolution face images with supplementary attributes. In *Proceedings of the IEEE conference on computer vision and pattern recognition*, pages 908–917, 2018.

A Implementation Details

The governing Navier-Stokes equations (1) were solved with a Finite-Volume approach, which naturally supports the staggered discretisation such that the velocity vector fields are stored at the cell faces, whereas the scalar pressure field is stored at the cell centers. All fluxes were computed to second order accuracy using a central difference scheme. The presented method was implemented using the tensor operation library *TensorFlow* [Abadi et al., 2016]. This framework supports the GPU based execution of various linear algebra operations, however does not support sparse matrix data at the time of this project. Consequently, a series of custom operations surrounding the linear solves for advection-diffusion and pressure in the PISO scheme were added to facilitate an efficient, GPU-based execution of the solver. The backpropagation gradients of the custom linear solves $Ax = b$ were linearised around their respective matrices and thus read as $A^T \hat{b} = \hat{x}$, where \hat{x} and \hat{b} represent the incoming and outgoing backpropagation gradients of the linear solve operation. This yields a solver that can flexibly change the number of steps unrolled during training (only limited by GPU memory and computation time), and account for any loss functions or network architectures. Access to our code is provided through the following GitHub page: <https://github.com/tum-pbs/differentiable-piso>

B Convolutional Neural Network

Our turbulence models are parameterised by a CNN, and thus formed by the kernel weights in each convolutional layer. Our setup utilises 7 layers with kernel sizes [7, 5, 5, 3, 3, 1, 1] and *leaky ReLU* activation functions. The input to the network consists of the velocity and pressure gradient vector fields, yielding 4 channels in total. The layers then operate on [8, 8, 16, 32, 32, 32] channels respectively and output a forcing vector field with 2 channels. Consequently, the network consist of $\sim 82 \times 10^3$ trainable weights contained in the kernels. Prior to training, the weights were initialised using the *Glorot Normal* initialisation. By the nature of the discrete convolution operation, the output size shrinks with each layer. At periodic boundaries this can be counteracted by padding the input with real data. At other boundaries, where no periodicity is enforced, no padding procedure is used on the input to avoid feeding unphysical data. In these cases, the output of the CNN does not coincide with the grid dimensions and is accordingly padded with zeros.

C Training Procedure

Our method trains neural networks to model the effect of turbulent motion. These effects are implicitly learnt from high-resolution DNS simulations by reproducing their behaviour. The networks were trained with a learning rate of 1×10^{-5} using the Adam optimizer, and a learning-rate decay factor of 0.4. We found that the training procedure was stable for learning rates in the neighbourhood of that value and also for different loss factors λ , however no extensive hyper-parameter tuning was performed. Contrary, we found the unrollment number s (see equation (4)) to have great effect on the training procedure. Newly initialised models can cause the accumulation of erroneous structures and subsequently solver divergence in long unroll times. To mitigate this effect, the models trained on more than 10 steps were initialised with a pre-trained network from a 10-step model. The parameter optimisations were run until no further significant decrease in loss values is observed.

D Large Eddy Simulation with the Smagorinsky Model

A series of tests were conducted to select an appropriate value for the Smagorinsky coefficient used in the isotropic decaying turbulence simulation in section 3. We ran simulations with our usual downscaling of $8\times$ in space and time and coefficients from $C_s = [0.17, 0.08, 0.02, 0.008, 0.002]$. The velocity-MSE of these simulations with respect to the DNS test-data after $100\Delta t$ were evaluated to $[12.21, 6.824, 4.320, 4.256, 4.364] \times 10^{-3}$. Based on that analysis, $C_s = 0.008$ was chosen for further consideration. This value is relatively low in comparison to other common choices, such as the default coefficient of $C_s = 0.17$ [Pope, 2000]. However, with the strictly dissipative behaviour of the Smagorinsky model, larger C_s lead to an overly powerful dampening of fine scale motions that quickly decreases the turbulence kinetic energy.